Magnitude Scaling of Early-Warning Parameters for the M_w 7.8 Tocopilla, Chile, Earthquake and Its Aftershocks

by M. Lancieri, A. Fuenzalida, S. Ruiz, and R. Madariaga

Abstract   We studied the correlation between the final event magnitude and four parameters obtained from the early portion of P and S phases for a set of high quality subduction events. These relationships are used in the framework of earthquake early-warning systems for real-time magnitude estimation. The investigated parameters are the low-pass-filtered peak displacement (PD), the integral of the velocity squared (IV2), and the predominant and characteristic periods (τ_p and τ_c). We created a dataset from the continuous records of the first two weeks following the 14 November 2007 M_w 7.8 Tocopilla (Chile) earthquake. The dataset includes 69 events with magnitudes greater than 4, among them the main event (M_w 7.8), the main aftershocks of M_w 6.7 occurred on November 15, and 4 events with magnitude greater than 6. The low-pass-filtered PD read on short P-phase and S-phase windows is well correlated with the final magnitude, confirming previous results. Indeed when examining 2-s time windows of P waves, we did not observe any saturation effect for magnitudes greater than 6.5; however, there is a slope change in the regression curve. A similar result is obtained from the integral of squared velocity computed over short windows around P and S waves. The characteristic and predominant periods are correlated with magnitudes up to M_w 6; but they clearly do not scale with the magnitude for the stronger events. Our observations offer insight into the feasibility of an early-warning system in Chile.

Introduction

The most critical problem for the development of an earthquake early-warning system (EEWS) is obtaining an estimate of the event size while it is still in progress. Nakamura (1988) proposed using information carried by the first few seconds of the P phase to estimate the event magnitude. In the last few years, several such techniques have been developed and implemented, based on empirical relationships between the event magnitude and parameters measured during the first seconds of the recorded signal. These early parameters are usually derived from the measure of P-phase frequency content (Nakamura, 1988; Allen and Kanamori, 2003; Wu and Kanamori, 2005a; Simons et al., 2006), peak values (Wu and Zhao, 2006; Zollo et al., 2006, 2007), and integral quantities (Bose et al., 2008; Festa et al., 2008).

In this article, we describe our investigation into the correlation between some of the early-warning parameters and the final event magnitude on a catalog of subduction events composed of the M_w 7.8 Tocopilla earthquake (14 November 2007) and its aftershocks. The Tocopilla event in northern Chile is a large thrust earthquake, located at 52 km depth and originated by the subduction of the Nazca plate beneath the South America plate. It occurred along the northern Chile seismic gap (Kelleher, 1972; Nishenko, 1985), and it broke a narrow (30–50 km) area of 130 km in length (Delouis et al.,

2009; Peyrat et al., 2010). Its rupture zone is contiguous with the northern bound of the area ruptured by the 1995 Antofagasta earthquake (Ruegg et al., 1996; Chlieh et al., 2004). Comprehensive studies of this event are found in Delouis et al. (2009) and Peyrat et al. (2010).

This event is an interesting case study in that it occurred in an area where a seismological and geodetic network was operating. This is a recent network installed in 2005–2007 by a combined effort of GeoForschungs Zentrum (Germany), Centre National de la Recherche Scientifique/ Institut National des Sciences de l'Univers (France), and Departamento de Geofisica of the Universidad de Chile in the framework of the International Plate Boundary Project Chile (IPOC) (Schurr et al., 2009).

Two reasons motivated this work. On the one hand, the Chilean subduction zone is one of the most active in the world; in the last century almost all of the cities along the subduction coast have experienced a mega earthquake or large subduction earthquake, and several triggered tsunamis (Lomnitz, 2004). The recent M_w 8.8 earthquake of 27 February 2010 is an example. Because the area is characterized by a high level of hazard, exposure, and vulnerability, there are very practical reasons to investigate the feasibility of implementing an EEWS in this area. On the other hand, the

IPOC network provided the first continuous near-source digital records of a strong subduction event and its aftershocks. Thus, we have a unique opportunity of studying the properties of the early-warning parameters on a homogeneous dataset in terms of tectonic environment, focal mechanism, and recording network. Moreover, the availability of broadband and strong-motion signals permits us to look at the data-processing effects and at the influence of the instrument on the computed parameters and the magnitude estimation. Finally, we will verify whether the results previously obtained by many authors on crustal events are confirmed by our dataset, composed of subduction earthquakes with depths between 20 and 50 km.

The Analyzed Parameters

Predominant and Characteristic Period of the P Phase

The predominant period parameter (τ_p) of the P phase introduced by Nakamura (1988), and subsequently adapted by Allen and Kanamori (2003), is defined as

$$\tau_p = 2\pi \sqrt{\frac{X_i}{Y_i}}, \tag{1}$$

where

$$X_i = \alpha X_{i-1} + x_i^2 \tag{2}$$

is the vertical component of the smoothed ground velocity squared and

$$Y_i = \alpha Y_{i-1} + \left(\frac{dx}{dt}\right)_i^2 \tag{3}$$

is the derivative of smoothed ground velocity squared. Allen and Kanamori (2003) and Olson and Allen (2005) observed a linear relationship between the maximum of τ_p measured over 3–4-s time windows of the P phase and the event magnitude. They used a dataset composed of events from southern California, Alaska, Taiwan, and Japan, with M_w ranging between 3 and 8.

Wu and Kanamori (2005b) proposed another parameter based on the P-phase frequency content, the so-called characteristic period τ_c:

$$\tau_c = 2\pi \sqrt{\frac{\int_0^{t0} u^2(t)dt}{\int_0^{t0} \dot{u}^2(t)}}. \tag{4}$$

In contrast to τ_p, which is computed recursively, τ_c is evaluated on a fixed time window of length t_0 (usually 3–4 s of the P phase). Even if these parameters have similar physical meanings, τ_p and τ_c give different results when evaluated on the same seismic data. This discrepancy seems to be related to the strong influence of the noise level before the P-phase arrival on the τ_p parameter (Shieh et al., 2008).

The correlation between τ_p, τ_c, and magnitude gave rise to a debate in the scientific community about the deterministic nature of earthquakes. Olson and Allen (2005) claimed that the final magnitude of an earthquake is controlled by the initiation process within the first few seconds of fracture. Rydelek and Horiouchi (2006) contested the existence of a correlation between these parameters and magnitude of earthquakes in Japan for events of $M_w > 6$.

Recently Wolfe (2006) and Yamada and Ide (2008) carefully studied the property of the predominant period. The main conclusion of their work is that the linear relationship between the predominant period and the strongest event ($M_w > 6$) cannot be related only to the source properties, but it derives from a combination of attenuation, site effect, and filtering effects.

The Low-Pass-Filtered Peak Displacement

A further parameter used for the real-time magnitude estimation is the low-frequency peak displacement (PD) introduced by Wu and Zhao (2006) and Zollo et al. (2006). The basic idea was to investigate the relationship between the peak displacement read on the first seconds of records, the hypocentral distance (R), and the event magnitude (M):

$$\log(PD) = A + BM + C\log(R). \tag{5}$$

There are several differences between the works of Wu and Zhao (2006) and Zollo et al. (2006). For example, Wu and Zhao (2006) read the PD on the vertical component of broadband instruments, while Zollo et al. (2006) use strong-motion data and read the PD on the modulus of the displacement. Moreover, Zollo et al. (2006) also computed the PD relationship on the S phase; Lancieri and Zollo, 2008 subsequently discussed the possibility of using the S-wave information for regional early-warning system applications. Hereinafter, PD will designate the parameter computed following Zollo et al. (2006).

The relationships between PD and the event magnitude have been investigated on Euro-Mediterranean and Japanese data. PD shows a good correlation with event size up to M_w 7, when read on the 4-s P-phase time window and on the S phase. A sort of saturation effect appears on PD read from a 2-s P-phase window. The PD versus magnitude relationships have been used in the design of a probabilistic and evolutionary code, now implemented on the southern Italy EEWS probabilistic and evolutionary early warning system (PRESTo; Lancieri and Zollo (2008); Iannaccone et al., 2009; Zollo, Amoroso, et al. 2009; Zollo, Iannaccone, et al. (2009)) PD correlation with magnitude, and the related saturation have been investigated by Nielsen (2007), Murphy and Nielsen (2009) using dynamic and kinematic arguments.

Integral of the Velocity Squared

Festa et al. (2008) proposed an integral quantity for the real-time magnitude estimation: the integral of velocity squared (IV2) is give as

$$IV2 = \int_t^{t+\Delta t} v^2(t)dt, \qquad (6)$$

where the integral is computed on a window of length Δt after the arrival time of the investigated phase t, and v^2 is the modulus of velocity squared evaluated on the three components. This parameter is very interesting because it is directly related to the energy radiated during the first seconds by the earthquake by the relation of Kanamori *et al.* (1993):

$$E_s = 4\pi \frac{r^2}{F^2 R_{\theta,\phi}^2} \rho c IV2. \qquad (7)$$

This parameter was first investigated for early warning applications by Festa *et al.* (2008). For the same Japanese dataset used to study PD versus magnitude relationships, IV2 saturates around M_w 6.5 when estimated on a 4-s P-phase time window and a 2-s S-phase time window.

Building the Catalog

Using the parameters described in the previous section, we evaluated the aftershock sequence of the M_w 7.8 subduction earthquake that occurred in Tocopilla (northern Chile) on 17 November 2007. We analyzed the continuous records acquired by the IPOC network to create the event catalog. We then analyzed the signals recorded from 14 to 28 November 2007, when the strongest events occurred.

IPOC is a permanent, continuously recording multi-parameter network of 17 sites covering the northern part of Chile (from Antofagasta to Arica), with a mean station spacing of 80 km. All sites are equipped with broadband seismometers and accelerometers. Additional instrumentation includes continuous Global Positioning System sensors, magnetotelluric instruments, and tiltmeters (Schurr *et al.*, 2009). In our study, we used the seven southernmost stations (Fig. 1a) located within 120 km of the area covered by the aftershocks distribution.

The catalog building is done in three steps: event identification (binding), location, and magnitude determination.

Event Identification and Location

The phase-arrival detection procedure is based on a picker algorithm developed by A. Lomax, C. Satriano and M. Vassallo (personal commun., 2009). This picker algorithm is an extension of the Baer and Kradolfer (1987) and Allen (1978) techniques; it is specifically designed to operate stably on continuous, real-time, broadband signals so as to avoid excessive triggering during large events.
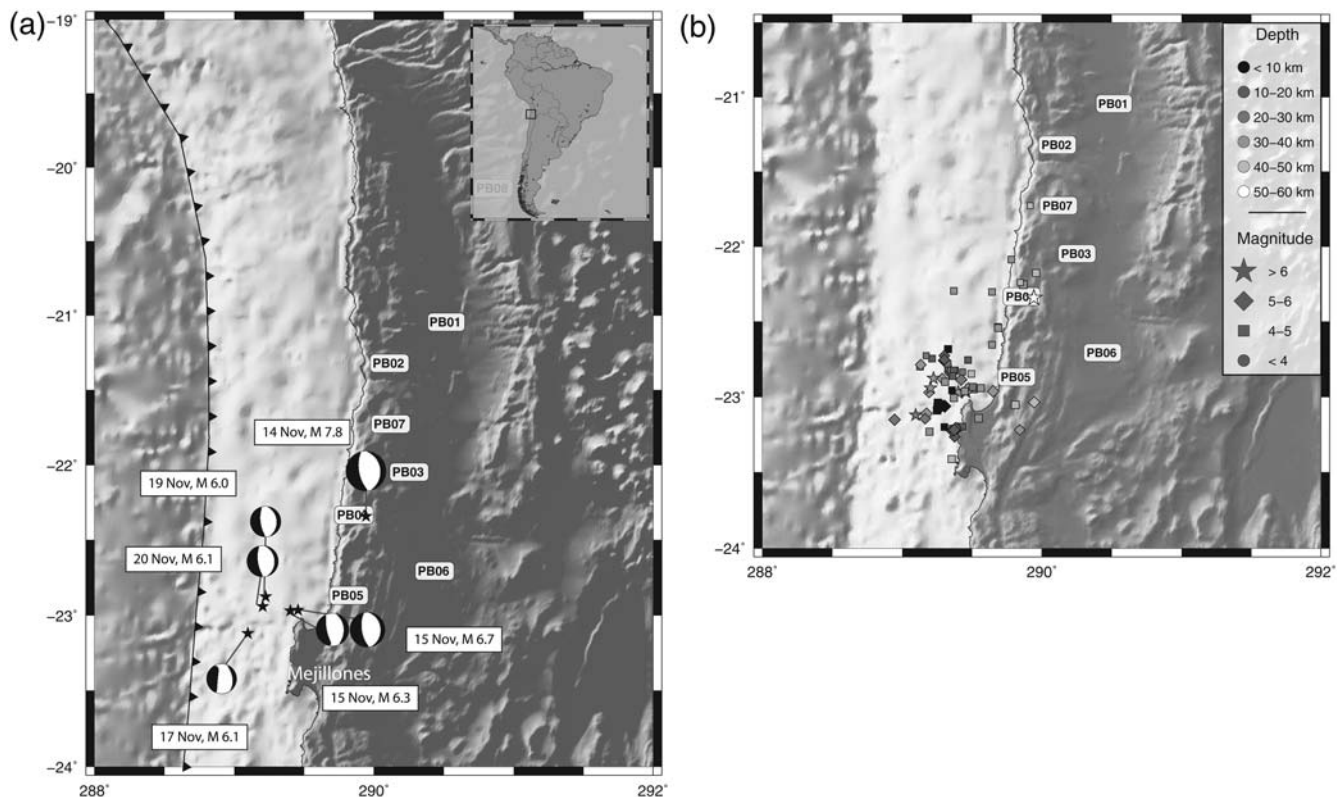

Figure 1. (a) IPOC network and main event location. The positions of the seven IPOC stations (PB01–PB07) and epicentral position (black stars) of the main events are indicated. The main event is located just beneath the PB04 station. During subsequent days, the seismicity migrated offshore of the Mejillones peninsula. All the events are thrust events; the plotted focal mechanisms were downloaded from the Global (formerly Harvard) centroid moment tensor catalog. (b) Geographic distribution of the 69 events used in the present study. The different symbols are the different magnitude classes; the gray scale shows the depth variation. The offshore events are shallower with respect to the inland earthquakes, but their locations are not well constrained because of poor azimuthal coverage.

The binding procedure analyzes the *P* arrivals at every station to determine whether they are compatible with propagation from a common source. We developed a simple technique, based on the coincidence of four to seven picks within a given time window (30 s for the IPOC network). We then automatically cut windows of 3 min (60 s before and 120 s after the *P*-phase) around each identified event.

To better constrain the event location, we manually revised the *P*-phase picking and manually picked the *S* phase. The events were located using the NLLoc software (Lomax *et al.*, 2001), using the vertically stratified velocity model obtained by Husen *et al.* (1999) from the study of aftershocks of the Antofagasta (M_w 8.0) earthquake of 30 July 1995.

From 14 November until 28 November 2007, we were able to detect, locate, and estimate the magnitude of 635 events. We identified 40 events on 14 November; this number is biased by the occurrence of several events very close in time whose signals overlap, so it was impossible to isolate the records, identify the *P*-phase and *S*-phase arrival times, and locate the events. We did not detect any foreshock before the main event of M_w 7.8. During the second day of activity (15 November), we detected and located 120 events. Among these, the main aftershock of M_w 6.7 occurred at 15:07 coordinated universal time (UTC). This event is located near the Mejillones peninsula (see Fig. 1a,b) at 25 km depth, and it was preceded by a 34-km-deep foreshock of M_w 6.2 at 15:03 UTC. In subsequent days, the seismic activity was mainly concentrated offshore of the Mejillones peninsula and along the coast in the northern rupture area; as shown in Figure 1a, the largest events ($M_w \geq 6$) are all located offshore. The event depths range from 10 to 52 km, although there is a large uncertainty on the depth estimations of offshore events because of poor azimuthal coverage.

Magnitude Estimation

The moment magnitude of the events was evaluated by inverting the displacement spectrum. On each component of ground motion, we inverted the low-frequency plateau, corner frequency, and quality factor using the Nelder–Mead algorithm (Nelder and Mead, 1965).

We assumed a Brune (1970) spectral model:

$$\Omega(f) = \exp\left(\frac{\omega r}{\beta Q}\right)\frac{\Omega_0}{1 + (\frac{f}{f_c})^2}, \tag{8}$$

where Ω_0 is the low-frequency spectral plateau and f_c is the corner frequency. The exponential term is the anelastic attenuation law, where Q is the quality factor; r is the hypocentral distance, and β is the *S*-wave velocity.

We evaluated the seismic moment using

$$M_0 = \frac{4\pi\beta^3\rho r\sqrt{\Omega_0(UD)^2 + \Omega_0(NS)^2 + \Omega_0(EW)^2}}{FR_{\theta,\phi}}, \tag{9}$$

where $\Omega_0(UD)$, $\Omega_0(NS)$, and $\Omega_0(EW)$ are the low-frequency plateau determined from the vertical, north–south, and east–

west components; ρ is the density; $F(\approx 2)$ is the free surface response; and $R_{\theta,\phi}(= 0.67)$ is the averaged radiation pattern. In our computation, all the dimensional quantities are expressed in international (SI) units.

The moment magnitude was then evaluated using the Hanks and Kanamori (1979) relationship:

$$\log(M_0) = 1.5M_w + 9.1. \tag{10}$$

The magnitude range of our catalog is 3–7.8; in Figure 2, we show the event magnitude distribution and the cumulative magnitude histogram. From the aftershock catalog, we evaluated the Gutenberg–Richter (1944) law,

$$\log N(M_w) = a + bM_w, \tag{11}$$

where M_w is the magnitude and $N(M_w)$ is the number of events with magnitude greater than M_w. The retrieved *b* coefficient is equal to 0.58 ± 0.30. This value is in good accordance with that calculated by Leyton, Ruiz, and Sepulveda (2009) for northern Chile. However, in most other studies, *b* is typically close to 1. The low *b* value may be related to two different factors: (1) our dataset is too small, or (2) the
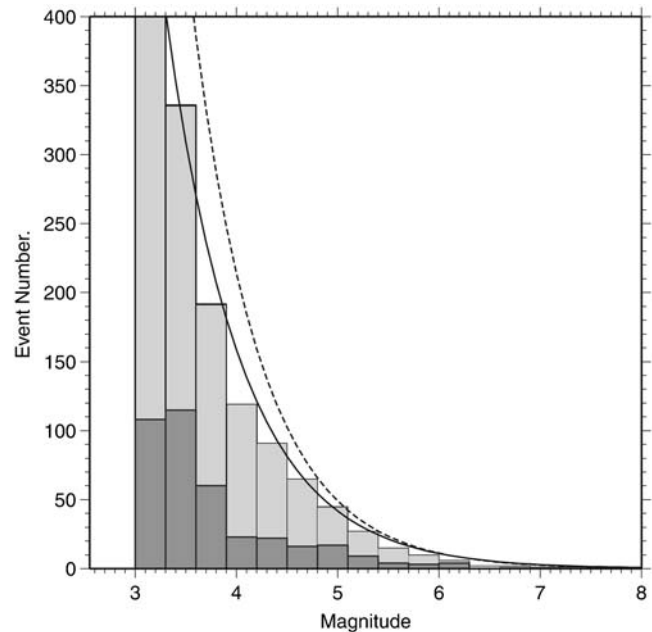

Figure 2. Magnitude distribution. The dark gray histogram is the number of events per magnitude bin, while the light gray is the cumulative histogram. Each bin has a size of 0.3 and represents the number of events with magnitude greater or equal to the magnitude value corresponding to the bin. The black line is the Gutenberg–Richter law evaluated on the retrieved dataset; the dashed line is the Gutenberg–Richter law retrieved by Leyton, Ruiz, and Sepulveda (2009) from the historical catalog for northern Chile. Because the number of events with $3 < M_w < 3.3$ is smaller than the number of events with $3.3 < M_w < 3.6$, it is then clear that we missed several events belonging to the first magnitude bin. This is due to the difficulty of isolating small events during the first few days of aftershocks.

minimum magnitude for completeness is too small (Feltzer, 2006). We think that the latter hypothesis is correct; we are not able to detect all the small events ($M_w \leq 3$) because it is not possible to read the *P* phase on the farthest stations, especially during the first days of activity when the *P* arrivals are merged to the coda of the stronger events.

Dataset

For this study, we selected all the events with magnitude greater than 4 for a total of 69 events with magnitude ranging from 4 to 7.8; for each event, we used the records obtained within 150 km from the hypocenter.

Several factors make this dataset an interesting case study: As indicated previously in this article, this is the first time that continuous records of a strong subduction event and its aftershocks are available. Moreover, the advantage of working with subduction earthquakes is that, even at larger distances, the signals are not very much affected by surface waves; it is then easy to isolate the *S*-phase wave packet. All the stations of the IPOC network that we used are installed on hard-rock sites; therefore, even at the farthest stations, the signal-to-noise ratio is high, and the *P*-phase and *S*-phase

arrivals are always very clear on the traces. Unlike in California, Taiwan, and Japan, there are no deep sedimentary basins in northern Chile; consequently, signals are not affected by spurious low-frequency trends. Finally, from the spectral analysis, we deduced that the anelastic attenuation effect on the signals is negligible in the investigated frequency range (Lancieri *et al.*, 2009)

In Figure 3, we show the acceleration waveform for four events that span the investigated magnitude range, each recorded at the closest station (hypocentral distances ranging from 52 to 82 km) and corrected for the distance: the main event (M_w 7.8), the main aftershock (M_w 6.8), and two aftershocks of M_w 6 and 5. The *P*-phase and *S*-phase windows used for the real-time magnitude estimation are highlighted in gray.

PD versus Magnitude Correlation

The first investigated parameter is the 3-Hz low-pass-filtered peak displacement. In Figure 4, we show the displacement modulus (corrected for the distance and filtered in a frequency band of 0.075–3 Hz using a 2-pole Butterworth filter) for the same records plotted in Figure 3. The PD is
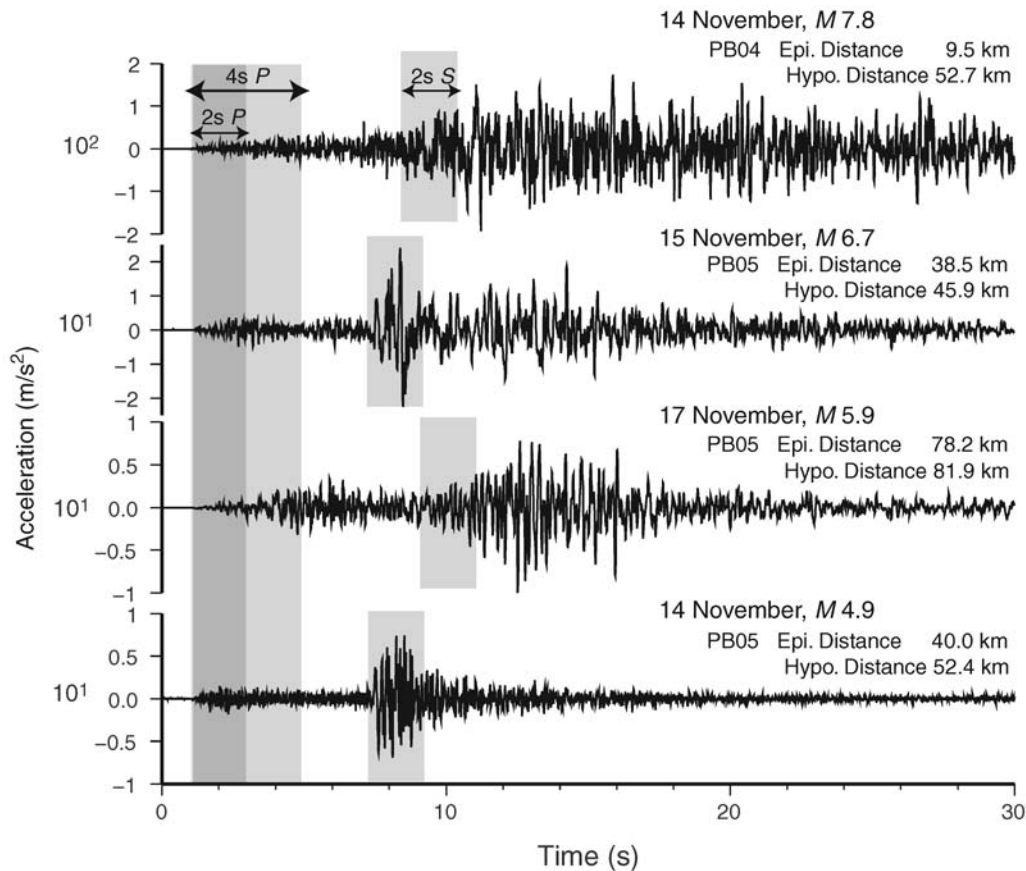

Figure 3. The north–south acceleration component for four events that span the investigated magnitude range. The amplitudes have been referred to a common distance of 1 km. The traces are aligned to the *P*-phase arrival time. For each event, we chose the closest station: PB04 for the main event, and PB05 for the other events. The variation in *S*-phase arrivals time is due to the different hypocentral distances. The signal windows used for real-time magnitude evaluation are highlighted in gray.
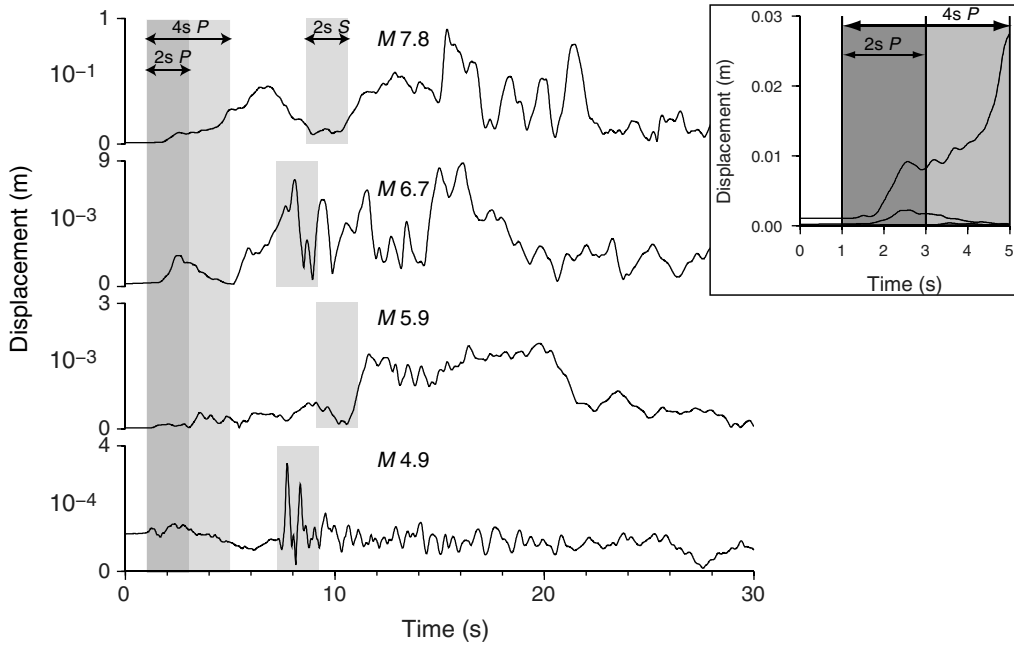
Figure 4. Vector composition of three components of displacement for the events displayed in Figure 3 at the same stations. The displacement modulus was computed from the strong-motion records, corrected for distance, doubly integrated, and filtered between 0.075–3 Hz. Inset shows a closer view of the 4-s P-phase windows, in which the main event and the M_w 6.7 aftershock are visible, while the amplitudes of the M_w 5.9 and 4.9 events are negligible.

defined as the maximum displacement in the 2-s and 4-s windows after the P-phase arrival and in the window of 2 s after the S-phase arrival; the signal portions used for PD reading are highlighted in gray. For simplicity, we will refer to those reading as PD_P^{2s}, PD_P^{4s}, and PD_S^{2s}, respectively. In the inset in Figure 4, we superimpose the first 4 s of P phase for all traces and plot them at the same scale. The only two visible traces are the M_w 7.8 and the M_w 6.7 events, whose amplitudes differ by a factor of 10. The traces of M_w 6 and 5 events are not visible on the plot because their amplitudes are negligible compared to those of stronger events. The close-up view on 4 s of the P phase clearly show that it is possible to distinguish the M_w 7.8 event from the smaller event at this temporal scale.

The inverted linear relationship is obtained from equation (5), correcting PD readings for hypocentral distance (we assume the C coefficient is equal to 1) and referring them to a common distance of 1 km:

$$\log(PD^{1\,km}) = aM_w + b. \tag{12}$$

In Figure 5, we show the correlation between PD and the event magnitude for strong-motion and broadband data, both filtered between 0.075 and 3 Hz. This filter window was fixed in agreement with previous studies (Wu and Kanamori, 2005a; Yamada *et al.*, 2007; Zollo *et al.*, 2007). Taking advantage of the availability of both broadband and strong-motion data, we also studied the effect of single or double integration to calculate the displacement. The broadband

records of the main event and the M_w 6.7 (15 November) aftershock are saturated at the closer stations. For these events, we used only the strong-motion data.

As a general remark, we did not observe clear saturation even on PD_P^{2s} readings but noted an evident change of the linear trend around M_w 6. This observation led us to investigate the slope variation of the linear relationship as a function of the magnitude range. In Table 1, we summarize the values for the a and b parameters for the PD read on different time windows using two different instruments. As expected, increasing the magnitude range decreases the value of the linear slope. This means that the larger the magnitude, the less predictive is PD. However, we note that parameters a and b differ for the two instruments; in particular, looking at the slopes evaluated in the magnitude range of 4–6, the value obtained using strong motion data is 0.69 ± 0.11, while the value obtained using the broadband data is 1.06 ± 0.14. The broadband result is closer to the expected value; in fact, in the lower magnitude range, the PD—magnitude relation can be interpreted as a local magnitude law. The misevaluation of slope on strong-motion data is a consequence of the low-frequency noise that dominates the displacement signal (obtained by a double integration of recorded accelerations) and has a remarkable influence on the P-phase amplitude. For events with magnitude less than 5, the 0.075–3 Hz filter did not adequately correct the baseline effect. We then decided to filter the displacements between 0.25 and 3 Hz.

In Figure 6, we evaluate the correlation between the magnitude and PD band-pass-filtered between 0.25 and
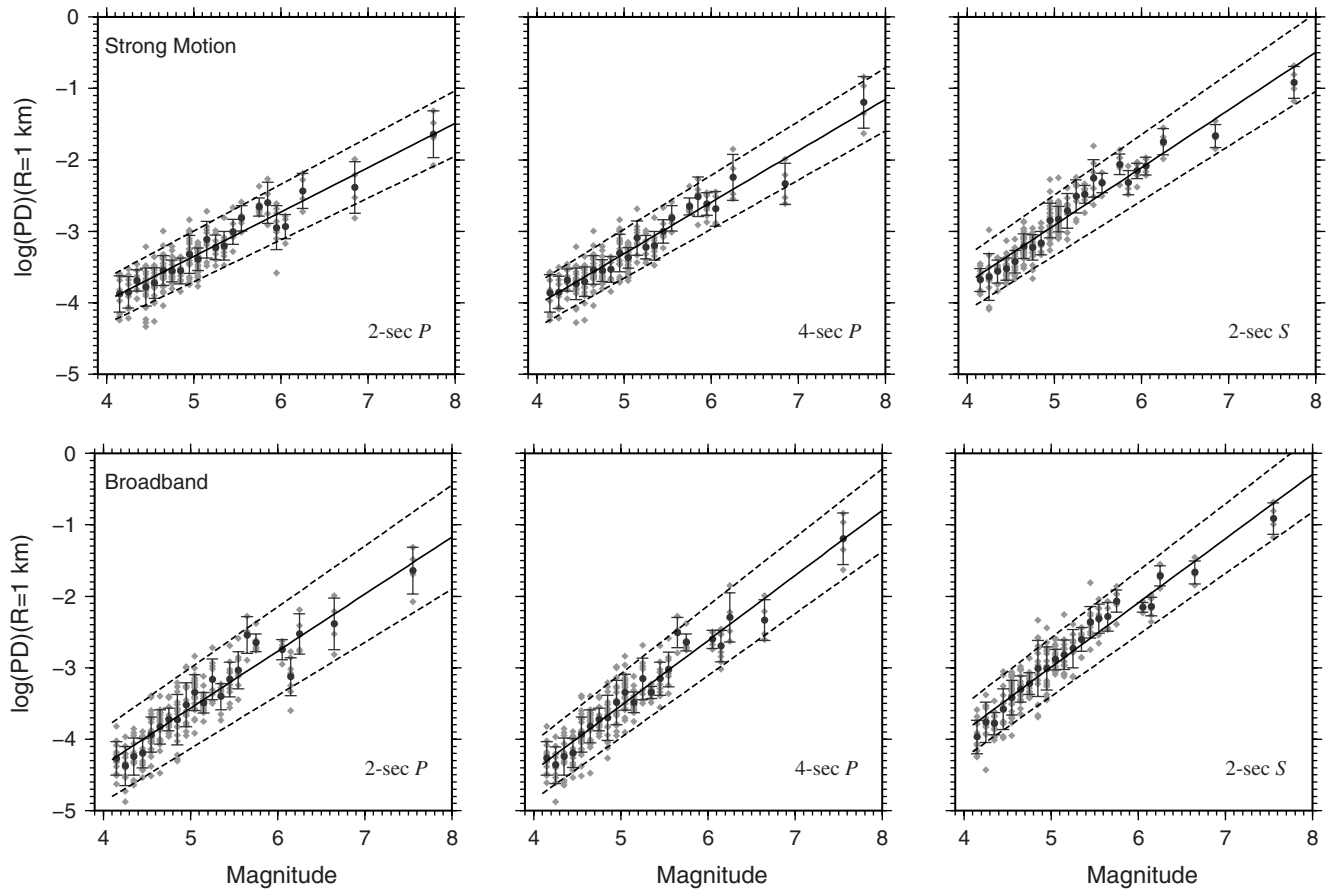
Figure 5. Correlation between band-pass (0.075–3 Hz) filtered peak ground motion value and magnitude. The logarithm of peak ground displacement normalized to a common reference distance of 1 km as a function of M_w is shown. (Top) PD read on strong-motion data; (bottom) PD read on broadband data. Black dots represent the peak average on the events with the same magnitude, plotted with the associated standard deviation. The gray diamonds are the peak values read on each record. The black solid lines are the best fit curves evaluated through a linear regression on the magnitude range of 4–8, plotted along with the statistical errors (dashed lines).

Table 1
Peak Displacement (PD) versus Magnitude, 0.075–3 Hz

| Magnitude	Strong Motion		Broadband	
	$b \pm \Delta b$	$a \pm \Delta a$	$b \pm \Delta b$	$a \pm \Delta a$
2 s *P* Phase				
4–6	0.69 ± 0.11	-6.81 ± 0.54	1.06 ± 0.14	-8.80 ± 0.70
4–7	0.62 ± 0.09	-6.45 ± 0.47	0.82 ± 0.14	-7.69 ± 0.72
4–8	0.62 ± 0.07	-6.45 ± 0.37	0.80 ± 0.11	-7.56 ± 0.59
6–8	0.66 ± 0.68	-6.80 ± 4.57	0.83 ± 0.60	-7.92 ± 3.91
4 s *P* Phase				
4–6	0.76 ± 0.08	-7.09 ± 0.43	1.07 ± 0.14	-8.85 ± 0.69
4–7	0.69 ± 0.08	-6.85 ± 0.43	0.91 ± 0.11	-8.08 ± 0.58
4–8	0.72 ± 0.07	-6.92 ± 0.36	0.91 ± 0.09	-8.09 ± 0.46
6–8	0.78 ± 0.96	-7.36 ± 6.50	0.94 ± 0.50	-8.37 ± 3.25
2 s *S* Phase				
4–6	0.97 ± 0.11	-7.85 ± 0.55	1.14 ± 0.06	-8.63 ± 0.31
4–7	0.86 ± 0.10	-7.22 ± 0.51	0.95 ± 0.09	-7.84 ± 0.48
4–8	0.81 ± 0.08	-6.95 ± 0.44	0.90 ± 0.08	-7.49 ± 0.42
6–8	0.62 ± 0.51	-5.80 ± 3.44	0.79 ± 0.40	-6.90 ± 2.60
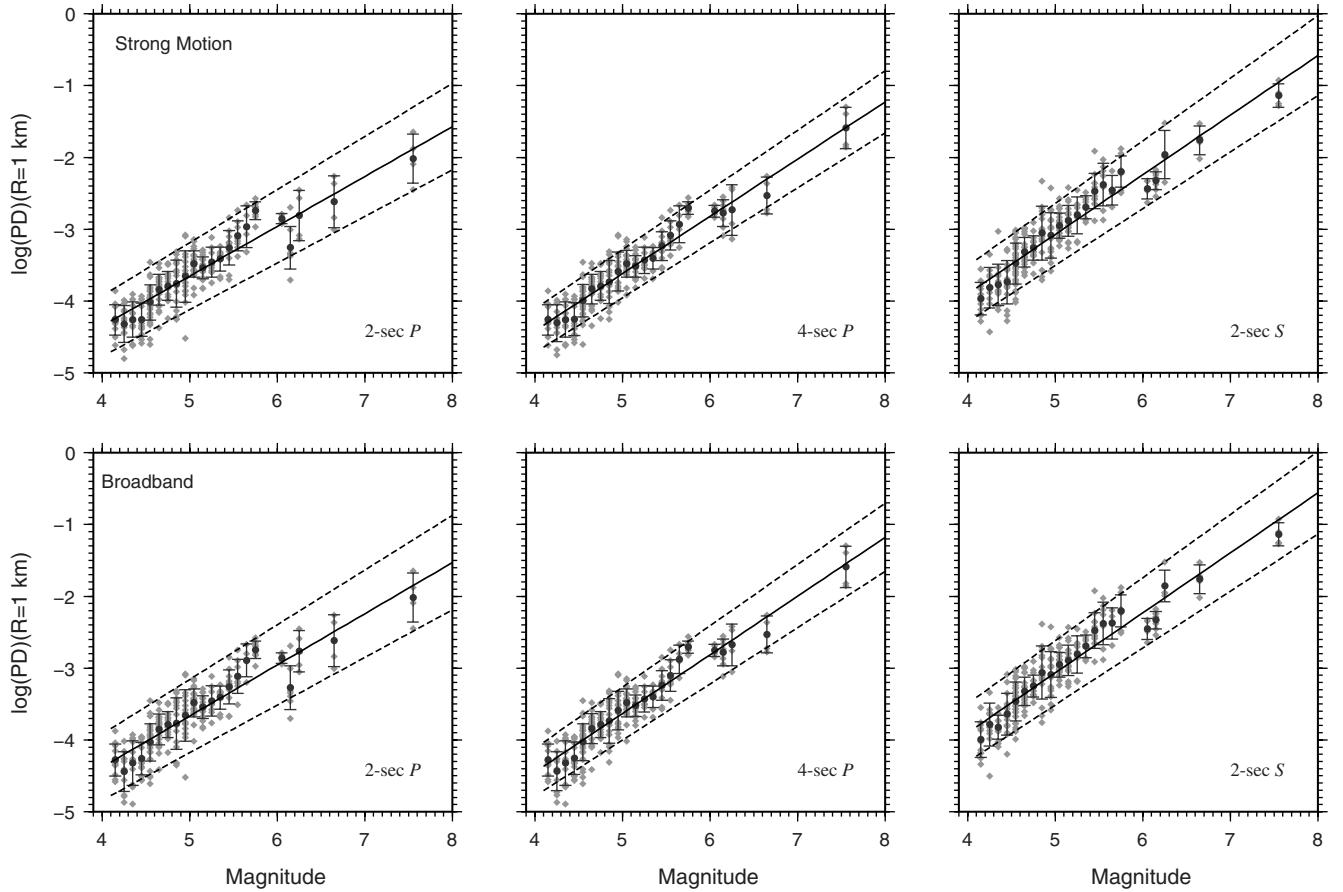
Figure 6.   The correlation between band-pass-filtered (0.25–3 Hz) peak ground motion value and magnitude. The logarithm of peak ground displacement normalized at a common reference distance of 1 km as a function of M_w is shown. (Top) PD read on strong-motion data; (bottom) PD read on broadband data. Black dots represent the peak average on the events with the same magnitude, plotted with the associated standard deviation. Gray diamonds are the peak values read on each record. The black solid lines are the best-fit curves evaluated through a linear regression on the magnitude range of 4–8, along with the statistical error (dashed lines).

3 Hz for strong-motion and broadband data. The coefficients are reported in Table 2. The linear trends retrieved for strong-motion and broadband records are comparable. However, the

0.25-Hz high-pass frequency reduces the PD level for the strongest events, enhancing the differences between the trends defined by the small and strong events. In conclusion,

Table 2
PD versus Magnitude, 0.25–3 Hz

Magnitude	Strong Motion		Broadband	
	$b \pm \Delta b$	$a \pm \Delta a$	$b \pm \Delta b$	$a \pm \Delta a$
2 s P Phase				
4–6	0.93 ± 0.09	-8.26 ± 0.47	0.98 ± 0.10	-8.50 ± 0.51
4–7	0.73 ± 0.11	-7.28 ± 0.59	0.75 ± 0.12	-7.43 ± 0.64
4–8	0.69 ± 0.09	-7.13 ± 0.48	0.71 ± 0.10	-7.23 ± 0.53
6–8	0.68 ± 0.53	-7.14 ± 3.48	0.68 ± 0.57	-7.12 ± 3.71
4 s P Phase				
4–6	0.94 ± 0.10	-8.31 ± 0.48	0.99 ± 0.10	-8.55 ± 0.52
4–7	0.80 ± 0.08	-7.61 ± 0.43	0.83 ± 0.09	-7.88 ± 0.47
4–8	0.80 ± 0.06	-7.61 ± 0.35	0.82 ± 0.07	-7.83 ± 0.38
6–8	0.80 ± 0.30	-7.82 ± 1.98	0.79 ± 0.30	-7.66 ± 1.94
2 s S Phase				
4–6	1.08 ± 0.07	-8.40 ± 0.37	1.08 ± 0.06	-8.42 ± 0.32
4–7	0.87 ± 0.10	-7.44 ± 0.52	0.88 ± 0.10	-7.48 ± 0.54
4–8	0.83 ± 0.08	-7.23 ± 0.45	0.84 ± 0.09	-7.24 ± 0.46

PD is well correlated with the final magnitude, confirming the results presented in previous studies (Wu and Zhao, 2006; Zollo *et al.*, 2006, 2007). Indeed, there is no evidence of saturation effect. The use of strong-motion records is suitable for looking at the strongest events, while the double integration of small events affects the determination of PD. The use of a 0.25–3-Hz band-pass filter is suitable for correcting the low-frequency trend evident on the smaller events, but it reduces the predictability of PD for the largest events. Using 0.25 Hz as the high-pass frequency, we are filtering above the corner frequency, removing the information coming from the source. For this reason, we think that it can be useful to use both the suggested filters: the 0.075–3-Hz filter to estimate magnitude for stronger events and the 0.25–3-Hz to look at the smaller events.

IV2 versus Magnitude Correlation

We next calculated the integral of the velocity squared (IV2). For the same four events shown in Figure 3, Figure 7 shows the behavior of the logarithm of the integral of squared velocity. We highlight 2-s and 4-s time windows after

P-phase and S-phase arrival, on which we calculate the IV2. As was done for PD values, the notation used for IV2 is $IV2_{phase}^{time}$ to distinguish the values read on the *P* and *S* phase in the different time windows.

It is interesting to note that IV2 behavior differs for each event: the main event shows a slow rise with respect to the smaller events, while the *S*-phase arrivals are very clear on the M_w 6.7 and M_w 5 events because they are characterized by a rapid growth of the $\log(IV2)Q_S$ value. However the amplitude of the main event is larger in the very first seconds of recording.

Figure 8 shows the relationships between IV2 and magnitude for strong-motion data, while Figure 9 shows the same relationships for the broadband records; both are filtered between 0.075 and 10 Hz and multiplied for the hypocentral distance squared. In both figures, we also plotted the correlation between magnitude and $\log(IV2)$ read on the entire *P*-phase and *S*-phase records. We set the *P* window duration as the time interval between the *P*-phase and *S*-phase arrivals. A critical point is to define the *S*-phase duration; we used the duration definition by Husid (1967), defining the end of *S* phase when 95% of the total energy amount is reached.
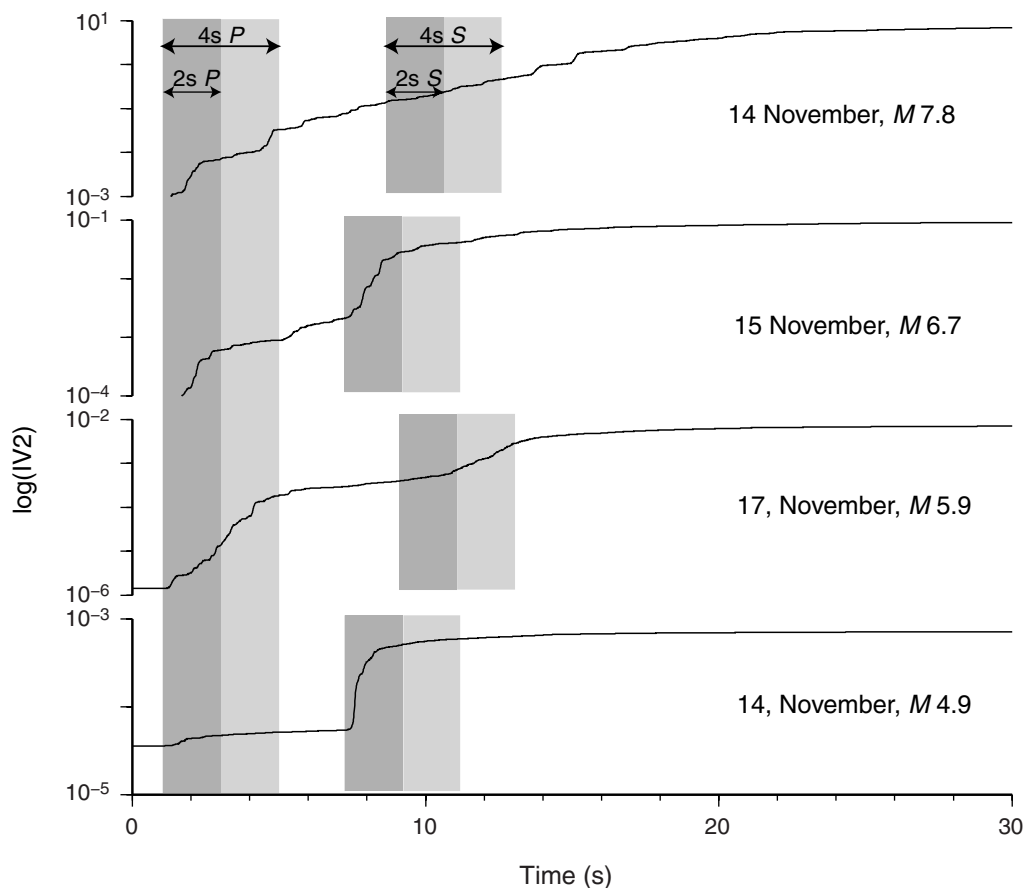

Figure 7. The logarithm of the integral of velocity squared for the events displayed in Figure 1. The cumulative integral plotted here was evaluated on the vector composition of velocity, obtained from the three components of the strong-motion records integrated once and band-pass-filtered between 0.075 and 10 Hz. Gray bars highlight the windows on which the IV2 integral (equation 6) was computed for real-time applications.
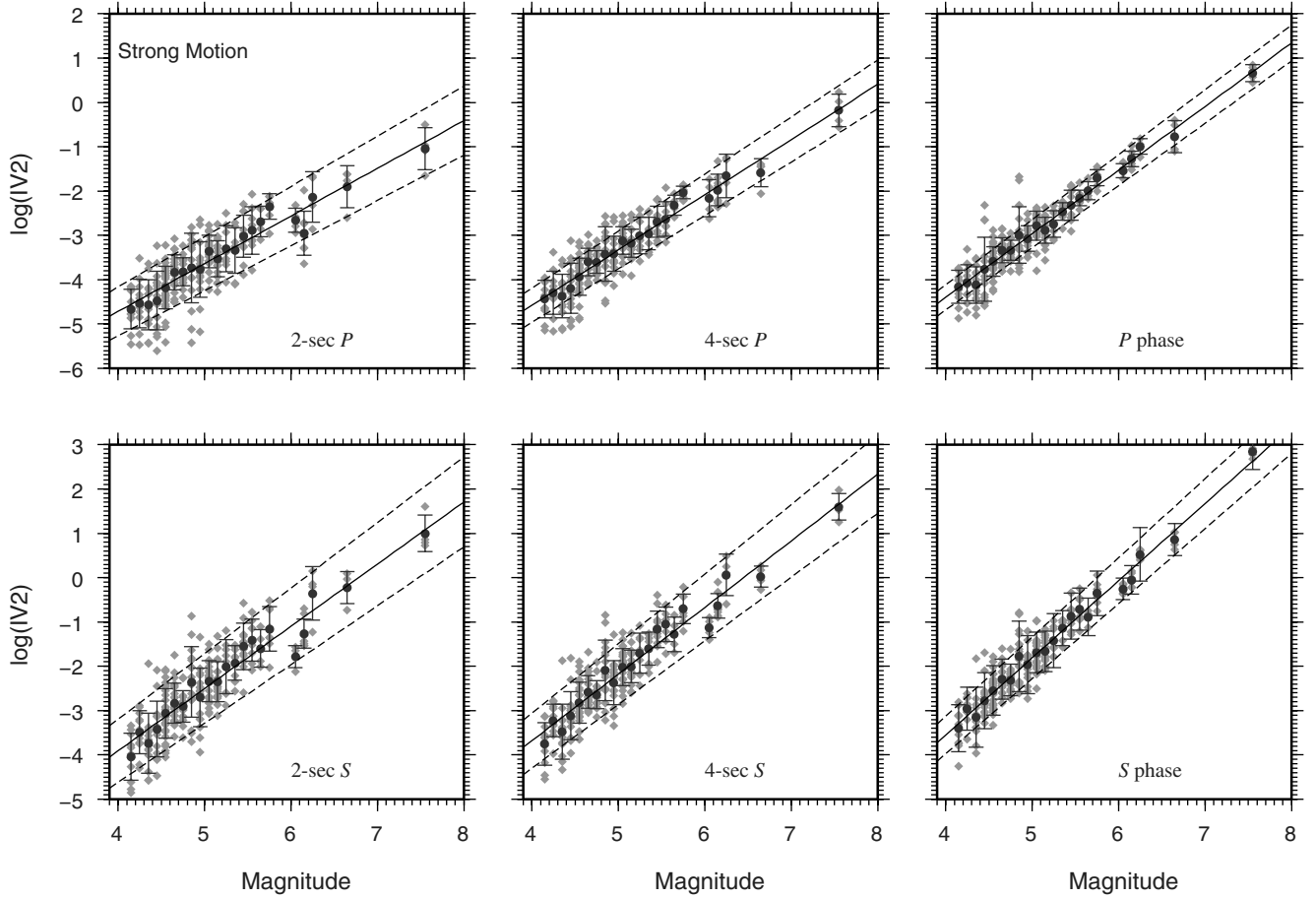
Figure 8. The correlation between IV2 evaluated from strong-motion records and magnitude. The integral of squared velocity as a function of M_w is shown. Traces have been filtered between 0.075 and 10 Hz and are corrected for the hypocentral distance, referred to a common distance of 1 km. (Top) IV2 read on P phase; (bottom) IV2 read on S phase. Black dots represent the IV2 average on events with the same magnitude, plotted with the associated standard deviation. The gray diamonds are the peak values read on each record; black solid lines are the best fit line evaluated through a linear regression on the magnitude range of 4–8, along with the statistical error (dashed lines).

As a general remark, IV2 appears to be well correlated with the final magnitude, and the results obtained for the two types of instrument do not differ significantly. $IV2_P^{2s}$ shows a break in linear relation around M_w 6, characterized by both slope and intercept changes (see Table 3 and Table 4). Such an effect is also visible on the $IV2_S^{2s}$ versus magnitude relationship. Increasing the time windows, $IV2_P^{4s}$ and $IV2_S^{4s}$ show a clear correlation with the final magnitude, and even the trend change appears to be less evident (Table 3 and Table 4).

In agreement with the theoretical model (see The Low-Pass-Filtered Peak Displacement section), the correlation between IV2, read on the entire P phase, and the magnitude (in the range of 4–6), is characterized by a slope of 1.43± 0.06, whereas the slope shown by the $IV2_{S\ phase}$ versus magnitude appears to be higher than the expected value. This effect is already visible on the $IV2_S^{2s}$ and $IV2_S^{4s}$ trends in the magnitude range of 4–6. This result is not surprising. In fact, to correctly determine the radiated energy, it is necessary to correct the records for anelastic attenuation

(Boatwright and Fletcher, 1984; Kanamori *et al.*, 1993) or for the finite bandwidth effect (Di Bona and Rovelli, 1988). The higher slope values observed for the IV2 correlation are probably related to the fact that we do not take into account such effects.

τ_p and τ_c versus Magnitude Correlation

The last parameters that we will discuss are the predominant and characteristic periods. It is important to remark that the analyzed data have not been recorded in the optimal conditions for the evaluation of τ (Allen and Kanamori, 2003; Wu and Kanamori, 2008). In fact, at larger distances, the attenuation can affect the tau measurement; nevertheless, because in this region anelastic attenuation is weak, our analysis includes the records located less than 150 km from the hypocenter.

Using the recursive definition given in equation 1, we compute τ_p for the four events shown in Figure 3. The predominant period is reported in Figure 10. The parameter
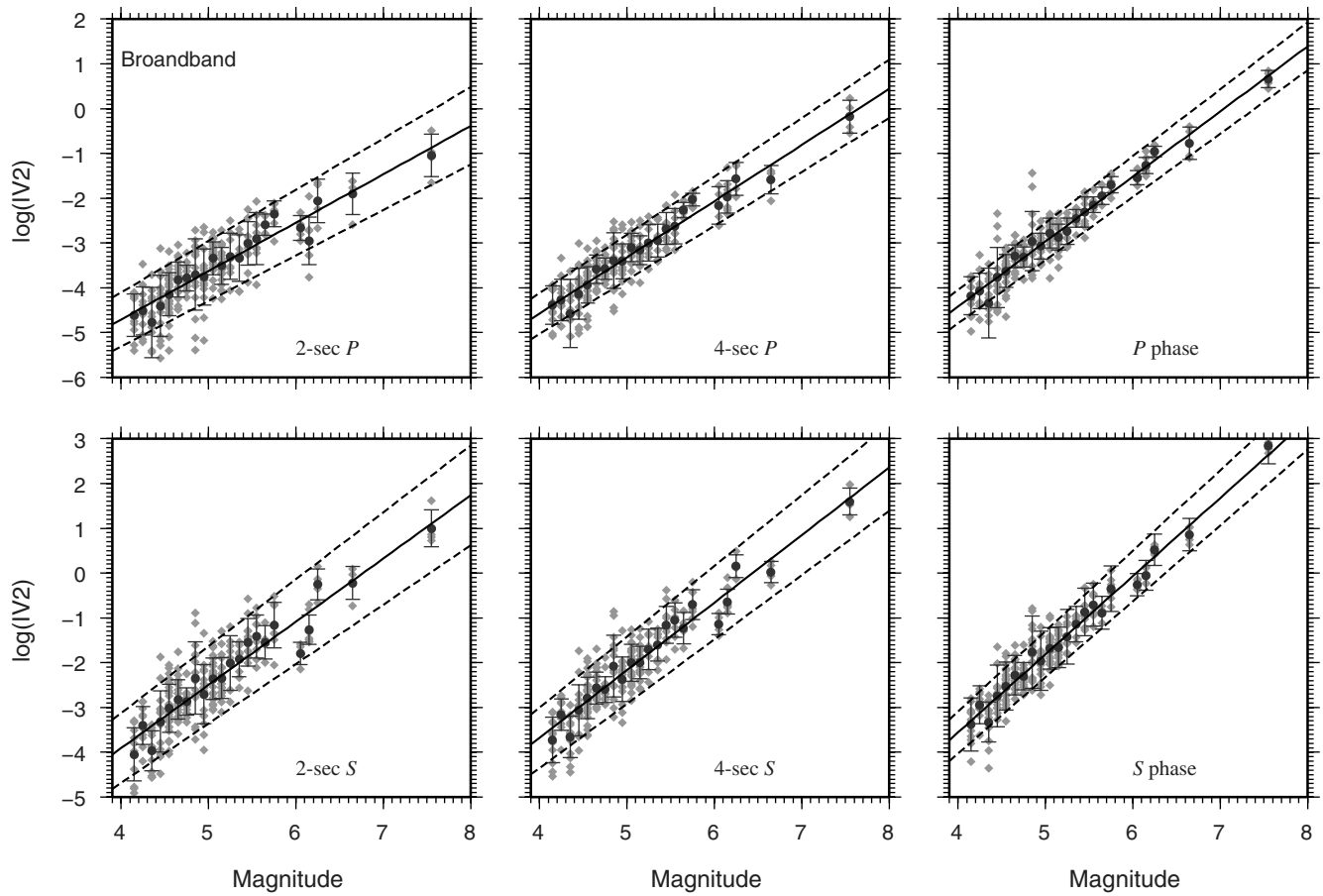
Figure 9. The correlation between IV2 evaluated from broadband records and magnitude. The integral of squared velocity as a function of M_w is shown. Traces have been filtered between 0.075 and 10 Hz and are corrected for the hypocentral distance, referred to a common distance of 1 km. (Top) IV2 read on P phase; (bottom) IV2 read on S phase. Black dots represent the IV2 average on the events with the same magnitude, plotted with the associated standard deviation. The gray diamonds are the peak values read on each record. The black solid lines are the best fit line evaluated through a linear regression on the magnitude range of 4–8, along with the statistical error (dashed lines).

Table 3
IV2 versus Magnitude, 0.075–10 Hz, *P* Phase

Magnitude	Strong Motion		Broadband	
	$b \pm \Delta b$	$a \pm \Delta a$	$b \pm \Delta b$	$a \pm \Delta a$
2 s *P* Phase				
4–6	1.34 ± 0.14	-10.29 ± 0.70	1.36 ± 0.17	-10.37 ± 0.84
4–7	1.11 ± 0.15	-9.20 ± 0.77	1.12 ± 0.16	-9.23 ± 0.85
4–8	1.08 ± 0.12	-9.02 ± 0.63	1.08 ± 0.13	-9.03 ± 0.69
6–8	1.13 ± 0.77	-9.49 ± 5.03	1.12 ± 0.84	-9.42 ± 5.52
4 s *P* Phase				
4–6	1.42 ± 0.12	-10.39 ± 0.61	1.44 ± 0.16	-10.48 ± 0.77
4–7	1.25 ± 0.10	-9.59 ± 0.55	1.27 ± 0.12	-9.65 ± 0.65
4–8	1.25 ± 0.08	-9.56 ± 0.44	1.25 ± 0.10	-9.59 ± 0.52
4–8	1.25 ± 0.47	-9.66 ± 3.07	1.23 ± 0.56	-9.52 ± 3.67
Entire *P* Phase				
4–6	1.49 ± 0.12	-10.38 ± 0.57	1.53 ± 0.16	-10.63 ± 0.78
4–7	1.44 ± 0.08	-10.18 ± 0.41	1.47 ± 0.10	-10.31 ± 0.53
4–8	1.43 ± 0.06	-10.14 ± 0.33	1.45 ± 0.08	-10.23 ± 0.43
4–8	1.38 ± 0.38	-9.81 ± 2.50	1.37 ± 0.42	-9.74 ± 2.76

Table 4
IV2 versus Magnitude, (0.075–10) Hz, S Phase

Magnitude	Strong Motion		Broadband	
	$b \pm \Delta b$	$a \pm \Delta a$	$b \pm \Delta b$	$a \pm \Delta a$
2 s S Phase				
4–6	1.66 ± 0.18	-10.73 ± 0.90	1.67 ± 0.22	-10.77 ± 1.08
4–7	1.42 ± 0.19	-9.62 ± 1.01	1.43 ± 0.21	-9.66 ± 1.11
4–8	1.40 ± 0.15	-9.52 ± 0.82	1.41 ± 0.17	-9.55 ± 0.90
4–8	1.61 ± 1.21	-11.02 ± 7.96	1.59 ± 1.35	-10.91 ± 8.83
4 s S Phase				
4–6	1.74 ± 0.18	-10.84 ± 0.89	1.75 ± 0.20	-10.87 ± 1.01
4–7	1.52 ± 0.17	-9.76 ± 0.88	1.53 ± 0.18	-9.80 ± 0.96
4–8	1.50 ± 0.13	-9.69 ± 0.71	1.51 ± 0.14	-9.71 ± 0.78
4–8	1.59 ± 0.97	-10.40 ± 6.35	1.58 ± 1.09	-10.29 ± 7.15
Entire S Phase				
4–6	1.78 ± 0.15	-10.69 ± 0.76	1.79 ± 0.18	-10.76 ± 0.89
4–7	1.69 ± 0.11	-10.25 ± 0.56	1.69 ± 0.12	-10.28 ± 0.63
4–8	1.74 ± 0.09	-10.51 ± 0.49	1.74 ± 0.10	-10.53 ± 0.54
4–8	1.99 ± 0.54	-12.22 ± 3.51	1.99 ± 0.54	-12.23 ± 3.52

that is supposed to be correlated with the final magnitude is the maximum read on a window of 4 s, measured after the P-phase arrival (time window highlighted in gray). All τ_p traces are plotted at the same amplitude scale. The τ_p amplitude for the M_w 5 event appears to be smaller with respect to that of larger events, but there is not an evident
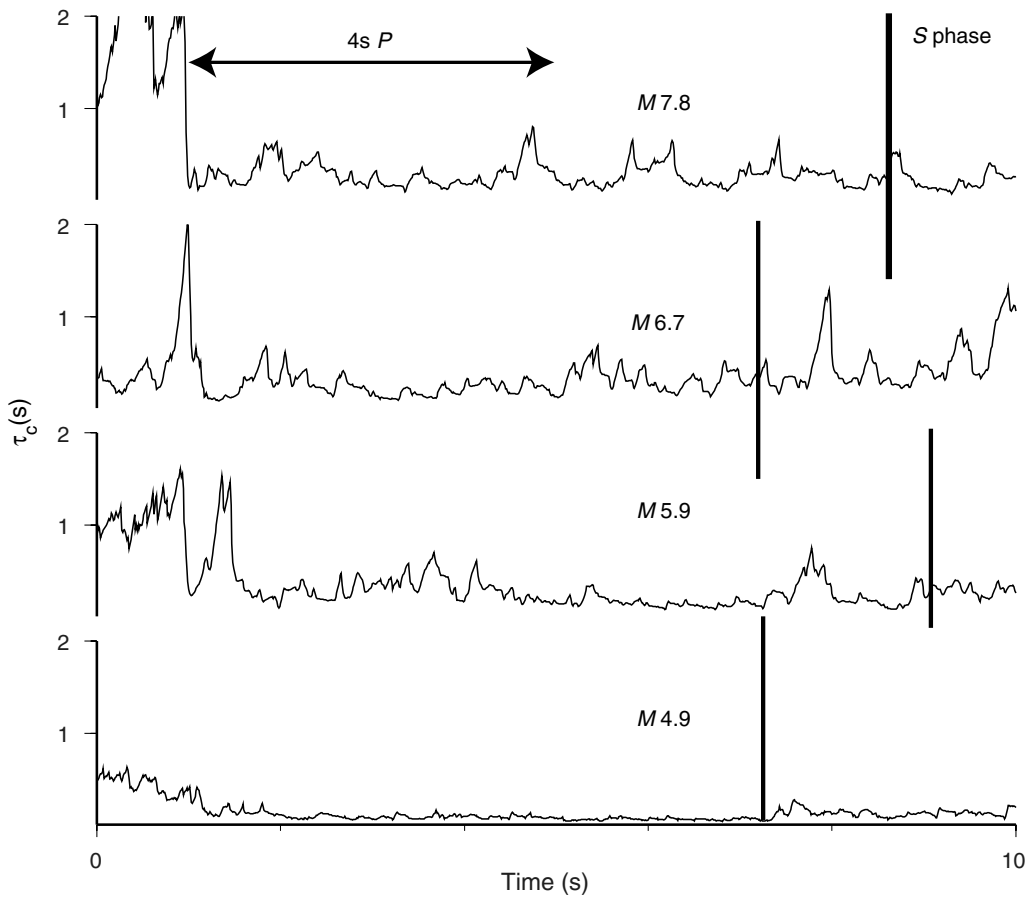

Figure 10. τ_p evaluated for the events of Figure 1. Note that, for all events, the y-axes have the same scale, and the peak amplitudes read in the 4-s windows (highlighted in gray) are comparable for the events with magnitudes greater than 5.9.
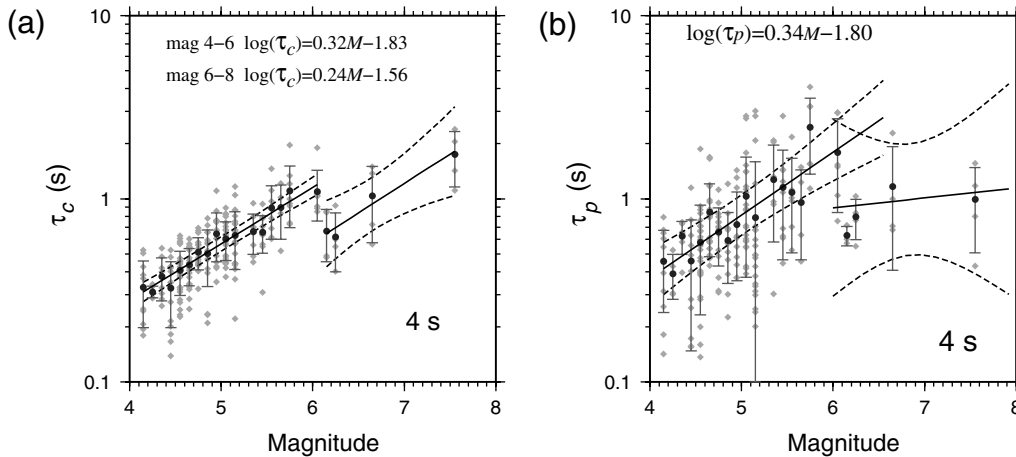
Figure 11. Correlation between τ parameters and event magnitude. (a) τ_c vs. magnitude. Black dots represent the peak average on each magnitude bin (associated standard deviations are included), and the gray diamonds are the peak values read on each record. The black solid lines are the best-fit curves evaluated through a linear regression on the magnitude ranges of 4–6 and 6–8. The dashed lines show the prediction limits (i.e., the 95% confidence interval for a new observation) that will be centered on $\hat{Y} = \log(PD^{1\ km})_k$ and whose length is given by $V[\hat{Y}] = s\{(1/n) + [(M_k - \bar{M})^2/(M_k - \bar{M}^2)]\}^2$, where s is the root of the mean square error, n is the number of observations, and $\bar{M}$ is the mean value of magnitude. (b) τ_p vs. magnitude. The symbols have the same meaning as in (a). The τ_p show a more dispersed behavior, and the linear regression in the M_w range of 6–8 does not have a statistical meaning.

scaling of τ_p for the strongest events. The characteristic period is given by a single value ($\tau_c = 4$), so it is not possible to show a figure similar to Figure 10 for this parameter.

In Figure 11a, we plot the relationships between the characteristic period (equation 4) and the event magnitude evaluated on a time window of 4 s after the *P*-phase arrival. The traces have been high-pass-filtered at 0.075 Hz. τ_c clearly scales with the final magnitude in the 4–6 range, and the linear trend is plotted in Figure 6, along with the 95% confidence interval for a new observation (Draper and Smith, 1998). The slope of 0.30 ± 0.05 is compatible with the values retrieved for the Japanese and Californian datasets (Wu and Kanamori, 2008) and for the European data (Zollo, Amoroso, *et al.*, 2009); the narrow confidence limits testify as to the good quality of the fit. Nevertheless, for magnitude values higher than 6, τ_c shows a weak dependence on the final magnitude. Indeed the limit of the retrieved relationship is that τ_c values for higher magnitude are comparable with those estimated for the smaller events. τ_c saturates for M_w 5.

The τ_p parameter (equation 1; Figure 11b) shows a large dispersion in the entire magnitude range; it is correlated with magnitudes in the 4–6 range, even if the large confidence limits imply a low statistical quality of the retrieved fit. For larger events there is no evident correlation with magnitude.

The τ_p versus magnitude fit for $M_w > 6$ (Figure 11b) does not have any statistical meaning; we plotted it to compare the trend defined by the confidence limits and the τ_p variability area obtained by Yamada and Ide (2008). This area has been determined by crossing the Olson and Allen (2005) relationship with the typical source duration versus magnitude correlation, and it is characterized by a horizontal bound around M_w 6.0. The resemblance between the two

results lead us to conclude that both τ parameters do not properly describe the source characteristic for the stronger Chilean events.

To better understand the τ_p behavior for the strongest events, in Figure 12 we compare the vertical component of the acceleration recorded at the PB04 station, located at a distance of 94 km, for an M_w 6 event with τ_p and the X and Y term in equation 1. The X term is a smoothed squared acceleration, and it can be related to the Arias intensity (Arias, 1970); while the Y term is a smoothed squared velocity, its formulation is similar to the IV2 parameter. On both X and Y terms, the amplitude increases with the *P*-phase and *S*-phase arrivals. The squared acceleration X, characterized by higher frequency content, is more attenuated than squared velocity Y. τ_p shows a sharp decay after the *P*-phase arrival, which is related to the good signal-to-noise ratio. However the peak amplitude read in the first second is comparable with the value read on an M_w 5 event (see Fig. 10). Looking at this example, we argue that, while the X and Y components are strongly related to the recorded ground motion, τ_p is only weakly connected to the actual signal. This can explain why it does not properly describe the magnitude of strong Chilean events.

Discussion

The results presented in this article open a new perspective on the feasibility of an early-warning system in Chile and other subduction zones. Nevertheless, some characteristics of Chilean seismicity should be taken into account to develop an effective EEWS in this area. The investigated relationships are used in the framework of regional EEWS. Those systems evaluate the expected ground-shaking level
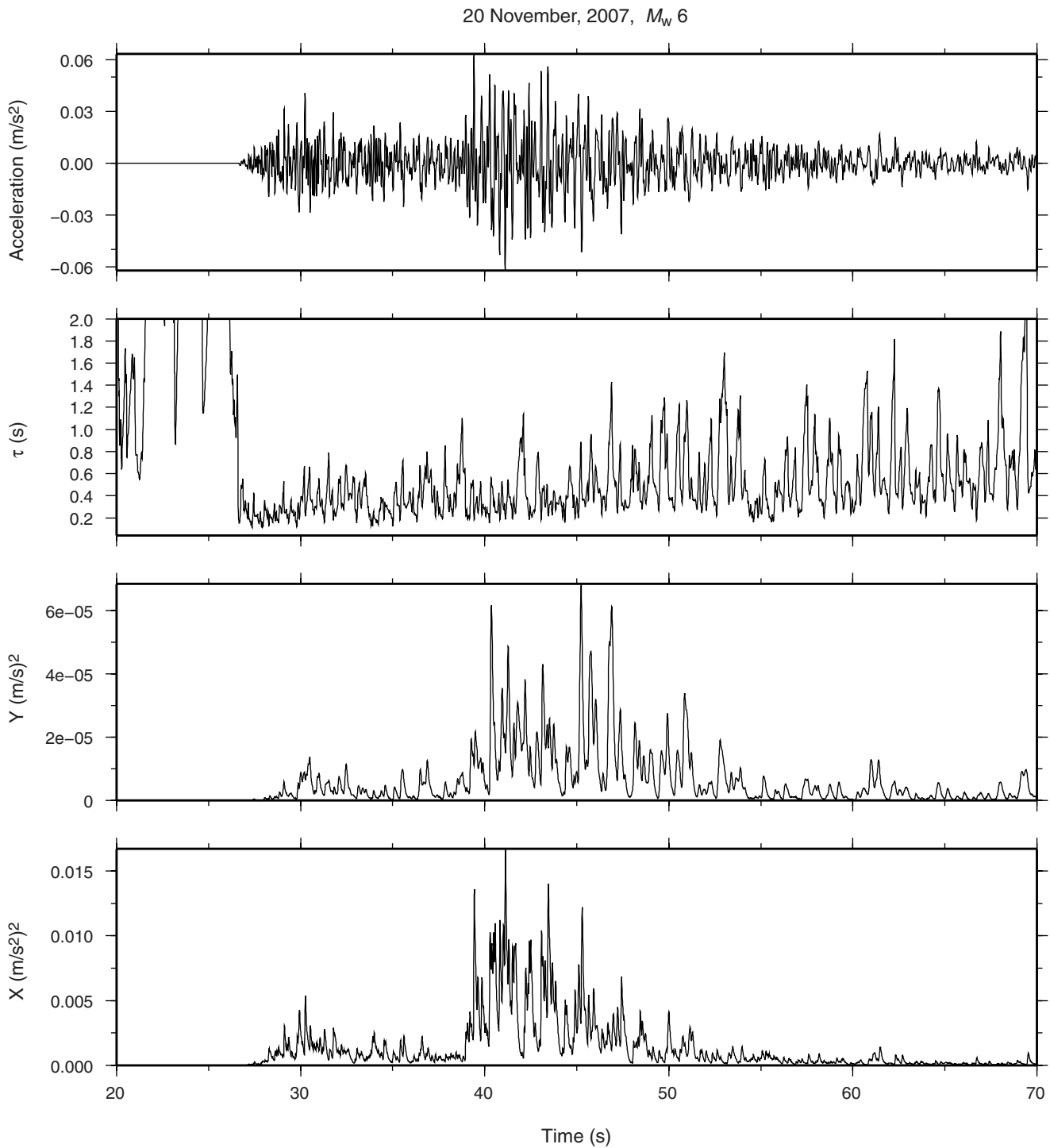
Figure 12.   The comparison between the vertical component of recorded acceleration, τ_p parameter, smoothed squared velocity Y, and smoothed squared acceleration X. The traces were recorded at the PB04 station after an event of M_w 6.0 occurred on 20 November 2007.

in real time, assuming a point-source model of the earth-quake source and isotropic wave amplitude attenuation. These assumptions may be inadequate, introducing a critical bias on the lead-time estimate (i.e., the time available for earthquake mitigation actions before the arrival of damaging waves) and on the prediction of the peak ground motion at the site of interest, as discussed in Zollo, Iannaccone, *et al.*

(2009). The use of the hypocentral distance in attenuation relationships is not always justified for Chilean earthquakes; in fact, the peak amplitude generated by these events is clearly correlated with the distance from each dominant asperity (Ruiz *et al.*, 2010).

Moreover, seismic risk in Chile is not only related to subduction earthquakes but also to inland intermediate-depth

earthquakes and shallow crustal events along the active western front of the Andes. In particular, intraslab earthquakes have a larger release of seismic energy, generate higher peak ground acceleration (PGA) value in the epicentral area, and are potentially more damaging than the subduction events (Saragoni *et al.*, 2004; Leyton, Ruiz, Campos, and Kausel, 2009). It is then crucial to be able to distinguish and characterize the different kind of events in real time and to have an appropriate attenuation relationship available. In this sense, it is important to provide an accurate, real-time estimate of earthquake depth. It is well known that the accuracy of depth location can be significantly improved by the use of *S* arrivals. However, to our knowledge, no real-time *S*-phase picker for EEW applications is currently available, and more research is required in this direction.

An alternative configuration is the site-specific EEWS, which consists of a single sensor or an array deployed in the proximity of the target site; the measurements of amplitude and predominant period on the initial *P* wave motion are used to predict the peak ground motion at the same site (Wu and Kanamori, 2005a). In this approach, the lead-time is given by the *S-P* time interval at the site; and, for subduction events, it should provide reasonable lead-time intervals. Of course, the bad correlation observed for the predominant period is a negative result for the feasibility of a site-specific approach in Chile. Nevertheless alternative onsite relations should be investigated (e.g., correlating PD, or IV2, with PGA or some other parameter related to the structural damage [Wu and Kanamori, 2005b; Zollo, Amoroso, *et al.*, 2009]) Also, for the site-specific approach, a complete study should integrate the investigation of the onsite correlations of seismic sequences related to the intraslab events.

Beyond these practical aspects, the observed correlations contribute to the debate on the causative link between the early parameters and the final event magnitude. In particular, it is very interesting to understand why we do not observe saturation on the subduction events we analyzed. A possible explanation for saturation has been given using the isochrones (Lancieri and Zollo, 2008; Murphy and Nielsen, 2009). An isochrone is defined as the set of points whose radiation arrives at a given station at a given time. The far-field radiation, recorded at a given station at a given time, can be expressed as a surface integral on the fault area delimited by the isochrone. The points on the isochrone do not irradiate simultaneously; the radiation emitted by the rupture front is delayed during the wave propagation, depending on the source-station geometry. The idea exposed in previous works is that the average area imaged by the 2 s *P* isochrones is larger or comparable with the final fault size for smaller events while it undersamples the fault plane associated with the strongest events, giving rise to saturation. Following this approach to explain our observation, for events up to M_w 6, the 2-s *P* isochrones sample a portion of fault comparable with the final size of fault; for higher magnitudes, the isochrones undersample the fault plane, but the sampled area

is large enough to permit us to distinguish the stronger events, explaining the observed slope change.

An alternative theory, argued by Nielsen (2007), concerns the fracture flow rate of elastic energy (G_c). The hypothesis is that an earthquake fracture that initiates with higher G_c has an increased probability of propagating to longer distances. As a consequence, the stress drop and/or the active slip surface have to scale with the seismic moment at the initial stage of seismic fracture. The verification of this hypothesis for our dataset will be the subject of a future work.

Conclusions

We analyzed four parameters proposed for the real-time magnitude estimation for EEWS application: low-pass-filtered peak displacement, the integral of the square velocity, and the predominant and characteristic periods. Their correlation with magnitude has been previously studied on several datasets, merging earthquakes generated in different tectonic settings and recorded with very different networks (Allen and Kanamori, 2003; Wu and Kanamori, 2005a; Zollo *et al.*, 2006, 2007). In this work, we investigated the behavior of those parameters on the aftershock sequence of the Tocopilla event of November 2007 (M_w 7.8) in northern Chile.

This dataset represents an interesting case study for several reasons: it is composed of subduction events recorded in the same tectonic setting and with all the same focal mechanisms and covering several orders of magnitude of actual interest for early-warning purposes (including the main event of M_w 7.8); the events have been recorded by a network equipped with both broadband and strong-motion instruments, giving us data of excellent quality; the stations are deployed on the area ruptured by the main event with epicentral distances ranging from 8 to 120 km (hypocentral distances from 50 to 150 km).

The first part of our work was the construction of the catalog. We detected and located the events, and we determined their moment magnitudes. Having continuous data, we extended our knowledge on the sequence, including the smaller aftershocks. Moreover, we have a good knowledge on the uncertainties of location and magnitude estimation of the earthquakes that compose the catalog; for this reason we did not introduce binning (typically 0.3 magnitude units wide) as used in the previous PD works, where event information was retrieved from existing catalogs and the magnitude was not always defined as moment magnitude.

In the second part, we investigated the correlation between the PD, IV2, τ_c, and τ_p parameters and the final magnitude. The PD parameter is confirmed as a good estimator of the magnitude for real-time applications. Contrary to the observation of Zollo *et al.* (2006; 2007), $PD_P^{2\,s}$ does not saturate at higher magnitudes, instead there is a visible step in the PD trend for higher magnitudes. The slope values, calculated for the entire magnitude range, are comparable to those retrieved in previous works on European and Japanese

data, while the intercepts are smaller (even considering the different reference distance). In the magnitude range of 4–6, the slope value is close to 1, so in this range the PD can the be interpreted as a local magnitude scale.

A similar result is obtained for the integral of the velocity squared (IV2) parameters. As for PD, the trends of IV2 do not show an evident saturation; furthermore IV2 seems not to be strongly influenced by the instrument. The statistical errors on the linear relation for IV2 are similar to those evaluated for the PD relationship (see Tables 1–4), making this parameter a possible alternative (or a complementary observation) to PD. The strength of IV2 is that it is related to the seismic radiated energy E_s, so it is a measure of a quantity directly related to the magnitude of an earthquake. Both of the period parameters, τ_p and τ_c, are correlated with the final magnitude in the 4–6 range but with different degrees of confidence. Nevertheless, for events in our dataset with magnitudes larger than 6, they are not good estimators of magnitude.

Data and Resources

Data used in this study are recorded by the International Plate Boundary Project Chile (IPOC) network, Centre National de la Recherche Scientifique/Institut National des Sciences de l'Univers (CNRS/INSU, France), Geo-Forschungs Zentrum (GFZ, Germany), and Departamento de Geofisica, Universidad de Chile (DGF, Chile). We are grateful for the free availability of data.

Acknowledgments

References

Allen, R. (1978). Automatic earthquake recognition and timing from single traces, *Bull. Seismol. Soc. Am.* **68,** no. 5, 1521–1532.

Allen, R. M., and H. Kanamori (2003). The potential for earthquake early warning in southern California, *Science* **300,** 786–789.

Arias, A. (1970). A measure of earthquake intensity, in *Seismic Design of Nuclear Power Plants*, R. J. Hansen (Editor), MIT Press, Cambridge, Massachusetts, 438–483.

Baer, M., and U. Kraudolfer (1987). An automatic phase picker for local and teleseismic events, *Bull. Seismol. Soc. Am.* **77,** no. 4, 1437–1445.

Boatwright, J., and J. B. Fletcher (1984). The partition of radiated energy between P and S waves, *Bull. Seismol. Soc. Am.* **74,** no. 2, 361–376.

Bose, M., F. Wenzel, and M. Erdik (2008). Preseis: A neural network-based approach to earthquake early warning for finite faults, *Bull. Seismol. Soc. Am.* **98,** no. 1, 366–382.

Brune, J. N. (1970). Tectonic stress and the spectra of seismic shear waves from earthquakes, *J. Geophys. Res.* **75,** no. 26, 4997–5009.

Chlieh, M., J. B. de Chabalier, J. Ruegg, R. Armijo, R. Dmowska, J. Campos, and K. L. Feigl (2004). Crustal deformation and fault slip during the seismic cycle in the north Chile subduction zone, from GPS and InSAR observations, *Geophys. J. Int.* **158,** 695–711.

Delouis, B., M. Pardo, D. Legrand, and T. Monfret (2009). The M_w 7.7 Tocopilla earthquake of 14 November 2007 at the southern edge of the northern Chile seismic gap: Rupture in the deep part of the coupled plate interface, *Bull. Seismol. Soc. Am.* **99,** no. 1, 87–89.

Di Bona, M., and A. Rovelli (1988). Effects of the bandwidth limitation of stress drops estimated from integrals of the ground motion, *Bull. Seismol. Soc. Am.* **78,** no. 5, 1818–1825.

Draper, N. R., and H. Smith (1998). *Applied Regression Analysis*, Wiley-Interscience, New York, 706 pp.

Feltzer, K. (2006). Calculating the Gutenberg-Richter b value, Fall Meet. Suppl., *Eos Trans. AGU,* **87,** no. 52, abstract S42C–08.

Festa, G., A. Zollo, and M. Lancieri (2008). Earthquake magnitude estimation from early radiated energy, *Geophys. Res. Lett.* **35,** L22307, doi 10.1029/2008GL035576.

Gutenberg, R., and C. Richter (1944). Frequency of earthquakes in California, *Bull. Seismol. Soc. Am.* **34,** 185–188.

Hanks, T. C., and H. Kanamori (1979). A moment magnitude scale, *Journ. Geophys. Res.* **84,** no. B5, 2348–2350.

Husen, S., E. Kissiling, and G. Asch (1999). Accurate hypocentre determination in the seismogenic zone of the subducting Nazca plate in northern Chile using a combined on-/off-shore network, *Geophys. J. Int.* **138,** 687–701.

Husid, R. (1967). *Gravity effects on the earthquake response of yielding structures*, Earthquake Engineering Research Laboratory, Califiornia Institute of Technology, Pasadena, California, 162 pp.

Iannaccone, G., A. Zollo, L. Elia, V. Convertito, C. Satriano, C. Martino, G. Festa, M. Lancieri, A. Bobbio, and A. Stabile, *et al.* (2009). A prototype system for earthquake early warning and alert management in southern Italy, *Bull. Earthq. Eng.*, doi 10.1007/s10518-009-9131-8.

Kanamori, H., J. Mori, E. Hauksson, T. Heaton, L. Hutton, and L. Jones (1993). Determination of earthquake energy release and M_L using TERRAscope, *Bull. Seismol. Soc. Am.* **83,** no. 2, 330–346.

Kelleher, J. (1972). Rupture zone of large South American earthquakes and some predictions, *J. Geophys. Res.* **77,** no. 11, 2087–2103.

Lancieri, M., and A. Zollo (2008). A Bayesian approach to the real-time estimation of magnitude from the early P and S wave displacement peaks, *J. Geophys. Res.* **113,** no. B12302, doi 10.1029/2007JB005386.

Lancieri, M., M. Fuenzalida, S. Ruiz, and R. Madariaga (2009). Magnitude scaling of the early displacement for the 2007, M_w 7.8 Tocopilla sequence (Chile), Fall Meet, Suppl., *Eos Trans. AGU* **90,** no. 52, abstract S13A–1725.

Leyton, F., J. Ruiz, J. Campos, and E. Kausel (2009). Intraplate and interplate earthquakes in Chilean subduction zone: A theoretical and observational comparison, *Phys. Earth Planet. In.* **175,** 37–46, doi 10.1016/j.pepi.2008.03.017.

Leyton, F., S. Ruiz, and S. A. Sepulveda (2009). Preliminary re-evaluation of probabilistic seismic hazard assessment in Chile: From Arica to Taitao Peninsula, *Adv. Geosci.* **7,** 1–7.

Lomax, A., A. Zollo, P. Capuano, and J. Virieux (2001). Precise, absolute earthquake location under Somma-Vesuvius volcano using a new three-dimensional velocity model, *Geophys. J. Int.* **146,** no. 2, 313–331.

Lomnitz, C. (2004). Major earthquakes of Chile: A historical survey, 1535–1960, *Seismol. Res. Lett.* **75,** 368–378.

Murphy, S., and S. Nielsen (2009). Estimating earthquake magnitude with early arrivals: A test using dynamic and kinematic models, *Bull. Seismol. Soc. Am.* **99,** no. 1, 1–23.

Nakamura, Y. (1988). On the Urgent Earthquake Detection and Alarm System (UrEDAS), in *Proc. 9th World Conf. on Earthquake Engineering VII*, Japan Association for Earthquake Disaster Prevention, Tokyo, Japan, 673–678.

Nelder, J. A., and R. Mead (1965). A simplex method for function minimization, *Comput. J.* **7,** 308–313.

Nielsen, S. (2007). Can earthquake size be controlled by the initial seconds of rupture?, in *Earthquake Early Warning Systems*, P. Gasparini, G. Manfredi, and J. Zschau (Editors) Springer-Verlag, Berlin, Germany, 9–19.

Nishenko, S. (1985). Seismic potential for large and great intraplate earthquakes along the Chilean and southern Peruvian margins of South America: A quantitative reappraisal, *J. Geophys. Res.* **90,** 3589–3615.

Olson, E. L., and R. M. Allen (2005). The deterministic nature of earthquake rupture, *Nature* **438,** no. 10, 212–215.

Peyrat, S., R. Madariaga, E. Buforn, J. Campos, G. Asch, and J. Vilotte (2010). Kinematic rupture process of the 2007 Tocopilla earthquake and its main aftershocks from teleseismic and strong motion data, *Geophys. J. Int.* **182,** no. 3, 1411–1430.

Ruegg, J., J. Campos, R. Armijo, S. Barrientos, P. Briole, R. Thiele, M. Arancibia, J. Cañuta, T. Duquesnoy, and M. Chang, *et al.* (1996). The $M_w = 8.1$ Antofagasta (north Chile) earthquake of July 30, 1995: First results from teleseismic and geodetic data, *Geophys. Res. Lett.* **23,** no. 9, 917–920.

Ruiz, S., E. Kausel, J. Campos, G. R. Saragoni, and R. Madariaga (2010). Identification of high-frequency pulses from earthquake asperities along Chilean subduction zone using strong motion, *Pure Appl. Geophys.*, doi 10.1007/s00024-010-0117-x (in press).

Rydelek, P., and S. Horiuchi (2006). Is earthquake rupture deterministic? *Nature* **442,** E5–E6 (20 July 2006), doi 10.1038/nature04963.

Saragoni, G. R., M. Astroza, and S. Ruiz (2004). Comparative study of subduction earthquake ground motion of North, Central and South America, in *13th World Conf. on Earthquake Engineering*, Vancouver, B.C., Canada, 1–6 August 2004, 104 pp.

Schurr, B., A. Asch, F. Sodoudi, A. Manzanares, O. Ritter, J. Klotz, G. Chong-Diaz, S. Barrientos, J.-P. Villotte, and O. Oncken, *et al.* (2009). The International Plate Boundary Observatory Chile (IPOC) in northern Chile seismic gap, *Geophys. Res. Abstr.*, **11,** abstract EGU2009-11040.

Shieh, J., Y. Wu, and R. M. Allen (2008). A comparison of τ_c and τ_p^{max} for magnitude estimation in earthquake early warning, *Geophys. Res. Lett.* **35,** L20301, doi 10.1029/2008GL035611.

Simons, F. J., B. D. E. Dando, and R. M. Allen (2006). Automatic detection and rapid determination of earthquake magnitude by wavelet multiscale analysis of the primary arrival, *Earth Planet. Sci. Lett.* **250,** 241–223.

Wolfe, C. (2006). On the properties of predominant-period estimators for earthquake early warning, *Bull. Seismol. Soc. Am.* **96,** no. 5, 1961–1965.

Wu, Y. M., and H. Kanamori (2005a). Rapid assessment of damage potential of earthquakes in Taiwan from the beginning of P waves, *Bull. Seismol. Soc. Am.* **95,** no. 3, 1181–1185.

Wu, Y. M., and H. Kanamori (2005b). Experiment on an onsite early warning method for the Taiwan Early Warning System, *Bull. Seismol. Soc. Am.* **95,** no. 1, 347–353.

Wu, Y. M., and H. Kanamori (2008). Development of an earthquake early warning system using real-time strong motion signals, *Sensors.* **8,** 1–9.

Wu, Y. M., and L. Zhao (2006). Magnitude estimation using the first three seconds of P-wave amplitude in earthquake early warning, *Geophys. Res. Lett.* **33,** L16312, doi 10.1029/2006GL026871.

Yamada, T., and S. Ide (2008). Limitation of the predominant-period estimator for earthquake early warning and the initial rupture of earthquakes, *Bull. Seismol. Soc. Am.* **98,** no. 6, 2739–2745.

Yamada, M., T. Heaton, and J. Beck (2007). Real-time estimation of fault rupture extent using near-source versus far-source classification, *Bull. Seismol. Soc. Am.* **97,** no. 6, 1890–1910.

Zollo, A., M. Lancieri, and S. Nielsen (2006). Earthquake magnitude estimation from peak amplitudes of very early seismic signals on strong motion records, *Geophys. Res. Lett.* **33,** L23312, doi 10.1029/2006GL027795.

Zollo, A., M. Lancieri, and S. Nielsen (2007). Reply to comment by P. Rydelek *et al.* on "Earthquake magnitude estimation from peak amplitudes of very early seismic signals on strong motion records,"*Geophys. Res. Lett.* **34,** L20303, doi 10.1029/2007GL030560.

Zollo, A., O. Amoroso, M. Lancieri, Y. Wu, and H. Kanamori (2009). An integrated regional and on-site early warning approach: Off-line application to the M_w 6.3, 2009 central Italy (L'Aquila) earthquake, *Eos Trans. AGU* **90,** no. 52, abstract S22A-01.

Zollo, A., G. Iannaccone, M. Lancieri, L. Cantore, V. Convertito, A. Emolo, G. Festa, F. Gallovič, M. Vassallo, and C. Martino *et al.* (2009). Earthquake early warning system in southern Italy: Methodologies and performance evaluation, *Geophys. Res.Lett.* **36,** no. 4, L00B07, doi 10.1029/2008GL036689.

Laboratoire de Géologie
Centre National de la Recherche Scientifique
Ecole Normale Supérieure
24 Rue Lhomond
75231 Paris Cedex 05, France
   (M.L., A.F., R.M.)

Departamento de Geofisica
Universidad de Chile
Blanco Encalada 2002
Santiago, Chile
   (S.R.)